NIPPON STEEL TECHNICAL REPORT No. 136 JULY 2026

Technical Report

Numerical Analysis of Milk Crown

Nobuhiro OKADA* Kouji TAKATANI

Abstract

Milk crown is a phenomenon in which a droplet bounces up in a crown-like shape when it falls into a liquid film. This beautiful fluid phenomenon occurs in a short time due to the balance between the liquid's inertial force and surface tension. Reproducing this phenomenon using computational fluid dynamics (CFD) is extremely difficult and has long been a challenging task. Multiphase flow analysis is difficult because the density difference between the gas and the liquid phases is approximately 1 000 fold. In recent years, the development of the Volume of Fluid method, which considers the free surface of a liquid, has improved the level of multiphase flow analysis. However, it remains difficult to accurately calculate the behavior of the gas-liquid interface while considering the surface tension. In this paper, numerical analysis techniques were reported to represent a milk crown on a computer.

1. Introduction

A milk crown is a beautiful natural phenomenon where a milk droplet, when dropped, bounces upward in a crown-like shape. Also called a Milk Drop Coronet, debate exists over whether it resembles a crown or a coronet, yet its beauty attracts many people. The time during which a milk crown forms and disappears is extremely short, lasting only a few milliseconds, making it difficult to observe its detailed behavior visually. The milk crown was first reported in an academic journal by A. M. Worthington in 1907,[1] and H. E. Edgerton captured stunning photographs of it in 1957.[2] Edgerton, a pioneer in strobe control technology, photographed and reported numerous phenomena occurring on the order of 1/1 000 of a second.

As high-speed photography technology has advanced, analysis of milk crown behavior has progressed, with numerous reports published. Deegan et al. analyzed high-speed camera footage, classifying milk crown morphologies into Crown Splash, Microdroplet Splash, and Peregrine Sheet, and organized them using the dimensionless Weber number We and Reynolds number Re.[3]

$$We = \frac{\rho D U^2}{\sigma}, \quad Re = \frac{\rho D U}{\nu} \tag{1}$$

Here, ρ is the liquid density, D is the droplet diameter, U is the droplet falling velocity, σ is the surface tension, and ν is the kinematic viscosity coefficient.

The formation of a milk crown involves a four-stage process. First, the droplet impacts the liquid film, forming an annular liquid film with a thickened upper edge. Next, this thickened upper edge undergoes flow instability, creating wavy regions of varying thickness. In the third stage, multiple protrusions called arms or corners grow from the thickened edge regions. In the fourth stage, the tips of these protrusions become rounded due to surface tension and detach from the protrusions. This fourth-stage shape is the iconic form of the milk crown, known as the Crown Splash. Microdroplet Splash is the phenomenon where minute droplets scatter before protrusions grow. Peregrine Sheet involves the formation of a cylindrical membrane bulge, but the protrusions do not grow sufficiently.

According to Deegan et al., Crown Splash occurs exclusively when the Reynolds number (Re) is less than 1 000 and the Weber number (We) is greater than 600. As Re increases, Microdroplet Splash accompanies it. Furthermore, Peregrine Sheet does not form when Re is 1 300 or less and We is less than 40. They report the conditions in Equation (2) as necessary for Crown Splash to occur. Thus, it is evident that the formation of a milk crown depends on the balance between the inertial force of the falling droplet and interfacial tension, causing its behavior to change.

$$We > 2.6 \times 10^4 \, Re^{-0.5} \tag{2}$$

Terzis et al. performed detailed imaging and quantitative analysis of milk crowns using urea aqueous solutions with adjusted surface tension.[4] They analyzed the number of arms formed based on the We number and liquid film thickness, reporting that fewer arms form as the We number decreases and the liquid film thickens. Furthermore, the thickness of the liquid film where the droplet impacts also significantly influences milk crown formation.

* Ph. D., General Manager, Head of Dept., Mathematical Science & Technology Research Lab., Advanced Technology Research Laboratories
20-1 Shintomi, Futtsu City, Chiba Pref. 293-8511

The difficulty in performing numerical fluid analysis of milk crowns lies in the challenge of reproducing free surfaces. Fluid analysis using methods like the finite difference method or finite volume method, which discretize space and calculate liquid motion in a Lagrangian manner, cannot completely suppress numerical diffusion. This leads to the problem of the interface becoming blurred due to transport. Consequently, many reported analyses of milk crowns use particle models[5] or the lattice Boltzmann method[6]. While these computational methods excel at representing free interfaces, they make coupled analysis with heat transfer or reactions difficult. In fluid analysis for steelmaking processes, analysis methods based on the finite difference method or finite volume method are also widely used. To incorporate the technology gained from tackling milk crown analysis, we undertook analysis using the finite volume method.

The method for handling free surfaces in the finite difference and finite volume methods employs the Volume of Fluid (VOF) method[7] developed by Hirt et al. The VOF method represents the interface in two-phase mixed flows (gas and liquid) by accurately transporting the volume fraction (VOF). Combining the VOF method with the level set method[8, 9] in an interface capture scheme enables precise free surface calculations. The level set method calculates a distance function representing the distance from the interface to represent it. This allows for accurate calculation of surface tension, which is particularly challenging to compute. Calculations for systems dominated by interfacial tension, such as droplets and bubbles, are highly sensitive to numerical analysis. Even minor differences in computational details can lead to vastly different results. Consequently, numerous computational methods have been reported, and the respective advantages and disadvantages of each technique have been discussed.[10] This paper presents results obtained by pursuing how beautifully a milk crown can be calculated, even if some aspects lack quantitative precision.

2. Mathematical Model

2.1 VOF method calculation approach

The equations to be solved for calculating a milk crown are the three equations shown in Equations (3) to (5). Here, ρ is the fluid density, $\mathbf{u}$ is the velocity vector, p is the pressure, μ is the viscosity coefficient, $\mathbf{g}$ is the gravitational acceleration vector, $\mathbf{F}$ is the external force vector, and φ is the volume fraction of the liquid phase (hereafter referred to as the volume fraction). The superscript T denotes the transpose matrix.

$$\frac{\partial(\rho\mathbf{u})}{\partial t}+\nabla\cdot(\rho\mathbf{u}\mathbf{u})=-\nabla p+\nabla\cdot(\mu(\nabla\mathbf{u}+(\nabla\mathbf{u})^{\mathrm{T}})+\rho\mathbf{g}+\mathbf{F} \quad (3)$$

$$\nabla\cdot(\rho\mathbf{u})=0 \quad (4)$$

$$\frac{\partial\varphi}{\partial t}+\nabla\cdot(\varphi\mathbf{u})=0 \quad (5)$$

Equation (3) is the momentum transport equation, Equation (4) is the mass conservation law, and Equation (5) is the fluid fraction transport equation. The unknowns are the velocity $\mathbf{u}$, pressure P, and fluid fraction φ, and calculations are performed using these three governing equations.

Figure 1 shows a schematic diagram of the calculation method in the VOF method. As shown in Fig. 1 (a), the fluid fraction φ is 1.0 when the liquid phase occupies 100% of the computational cell and 0.0 when the gas phase occupies 100%. The gas-liquid interface is contained within cells where φ is $0<\varphi<1$.

Figure 1 (b) shows the VOF method calculation flowchart and explains the overall computational flow. In the standard VOF method, both the gas phase and liquid phase are calculated using a single-fluid model represented by the same velocity field. As initial conditions, the initial liquid phase distribution is set by the fluid fraction, and for the milk crown case, a velocity is assigned to the falling droplet. Subsequently, Equations (3) to (5) are computed temporally at a small time interval Δt. The computational sequence is as follows: first, Equation (5) is used to calculate the fluid fraction φ^{n+1} at the next time step. Next, using the obtained fluid fraction, the physical properties (such as density and viscosity) for each cell are computed, and then Equation (3) is used to calculate the velocity at the next time step. However, since there is no guarantee that the velocity at the next time step satisfies the conservation law in Equation (4), the pressure and velocity are corrected to satisfy Equation (4). Several techniques are required to perform milk crown calculations. The method deemed appropriate among those investigated by the authors is described in the next section.

2.2 Volume fraction transport calculation method

The discretization of Equation (5) is shown in Equation (6). The superscript n indicates the value at the current time, and n+1 indicates the value after Δt seconds.

$$\frac{\varphi^{n+1}-\varphi^{n}}{\Delta t}+\nabla\cdot(\varphi^{n}\mathbf{u}^{n})=0 \quad (6)$$

To explain the calculation method of Equation (6), **Fig. 2** shows a schematic diagram of variable placement in fluid analysis using the finite volume method. φ and velocity U are set at the cell center,

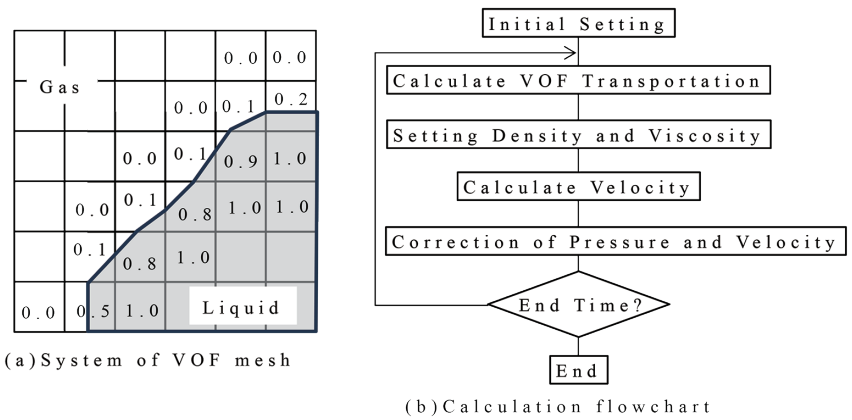

Fig. 1 Schematic diagram of VOF method

with the flow velocity at the cell interface denoted as U_f. Figure 2 shows a simple left-to-right flow, with the left element being the upstream side. The upstream side is denoted by subscript U, the center by C, and the downstream side by D. φ_C at the next time step is calculated from Equation (7).

$$\varphi_C^{n+1} = -\Delta t(\varphi_{fD}^n U_{fD}^n S_D - \varphi_{fU}^n U_{fU}^n S_U)/V + \varphi_C^n \quad (7)$$

Here, S is the interface area, and V is the cell volume. The change in φ_C is the difference between the value flowing out of the cell and the value flowing into it. While the interface velocity is obtained from the velocity calculation results, the problem arises in how to set the interface value φ_f. Simply using linear interpolation from the cell center might seem sufficient, but in this case, unphysical oscillations occur, necessitating a solution. For example, apply an upwind difference for stabilization. This method uses the value from the upstream cell in the flow for the interface. Applying first-order upwind scheme to the case in Fig. 2 yields Equation (8).

$$\varphi_C^{n+1} = -\Delta t(\varphi_C^n U_{fD}^n S_D - \varphi_U^n U_{fU}^n S_U)/V + \varphi_C^n \quad (8)$$

While upstream differentiation enables the transport quantity to be calculated with a smooth distribution, it introduces the problem of numerical diffusion, which remains a significant challenge in fluid analysis today. **Figure 3** illustrates numerical diffusion: (a) ideal transport and (b) a case where numerical diffusion occurs. At time n=1, the transport quantity is 1.0 in the second cell from the left, with all other cells set to 0.0. When transporting from left to right, without diffusion, the transport should propagate downstream with the width of the cell at n=1, as shown in Fig. 3(a). However, when first-order upwind scheme is applied, transport propagates downstream prematurely before reaching the interface, as shown in Fig. 3(b), spreading out as if it were diffusing. This is the numerical phenomenon known as numerical diffusion. When the transported quantity is a volume fraction, the gas-liquid interface becomes increasingly blurred as the calculation progresses. To solve this problem, many interface capturing methods have been developed.

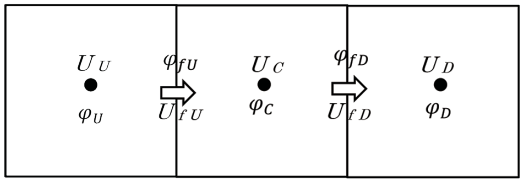

Fig. 2 Coordinate system of control volume in fluid dynamics

This time, the interface capture method employed was the CICSAM (Compressive Interface Capturing Scheme for Arbitrary Meshes) method.[10] The CICSAM method was a significant catalyst for the major advancement of the VOF method, and compared to other new methods, there was no significant difference.

The transport calculation of volume fraction is significantly influenced by the time integration method. Equation (8) is a simple method that explicitly calculates the value at time n+1 from the value at time n. When the Courant number is small, around 0.1, the calculation is feasible. The Courant number Cr is expressed as $Cr = U\Delta t/\Delta x$. Here, U is the flow velocity and Δx is the mesh length. If transport due to flow exceeds the mesh length in a single step, the calculation becomes unstable. Therefore, to perform stable calculations, the time step must be reduced, increasing computation time. Furthermore, since volume fraction calculations may fail, high-precision calculations are preferable. In this study, time integration was performed using the Crank-Nicolson method shown in Equation (9).

$$\frac{\varphi^{n+1}-\varphi^n}{\Delta t} = -\frac{1}{2}\{\nabla\cdot(\varphi^n \mathbf{u}^n) + \nabla\cdot(\varphi^{n+1}\mathbf{u}^n)\} \quad (9)$$

Equation (9) requires iterative computation because the right-hand side includes values from the next time step. Consequently, it requires more computation time than explicit methods but allows for a larger Courant number. However, to maintain computational accuracy, the Courant number must be less than or equal to 1.

Figure 4 shows a schematic diagram of the CICSAM method and explains the discretization method for the advection term in the CICSAM method. In the CICSAM method, the advection term is calculated as shown in Equation (10).

$$\nabla\cdot(\varphi\mathbf{u}) = \gamma(\theta)[\text{BD Scheme}] + (1-\gamma(\theta))[\text{HR Scheme}]$$
$$\gamma(\theta) = \frac{\cos(2\theta)+1}{2}, \quad \theta = \arccos(\mathbf{n}\cdot\mathbf{n}_\varphi) \quad (10)$$

Here, $\mathbf{n}$ is the unit normal vector perpendicular to the cell interface, and $\mathbf{n}_\varphi$ is the unit normal vector of the gas-liquid interface. $\gamma(\theta)$ is defined such that when the gas-liquid interface and the cell interface are parallel, as shown in Fig. 4(a), $\gamma(\theta)=1$, and the BD Scheme becomes 100% in Equation (10). The BD Scheme is the Bounded

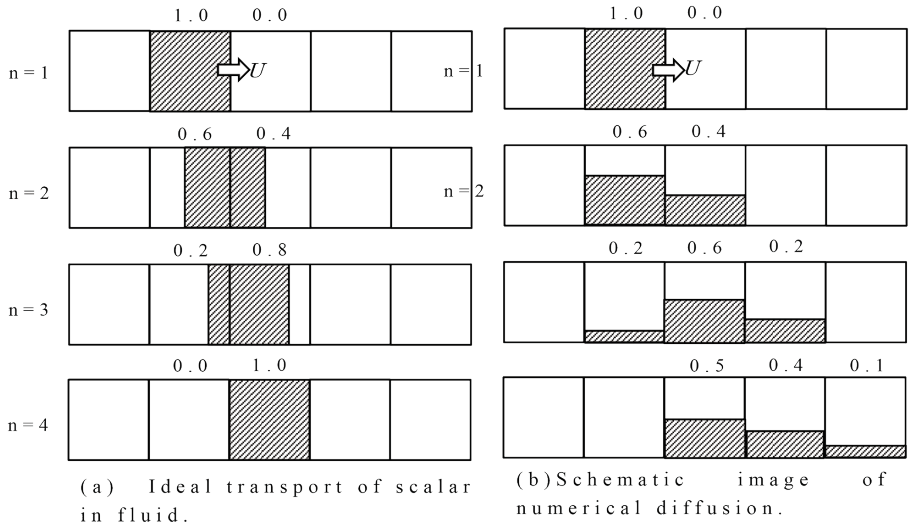

Fig. 3 Schematic image of numerical diffusion

Downwind Scheme, a method that adopts the downwind value. In Fig. 4(a), the value φ_{fU} at the cell interface of interest is taken as φ_U from the upstream cell using the first-order upwind scheme. However, using φ_U results in transporting the volume fraction downstream before the gas-liquid interface reaches the cell interface of interest. To avoid this, the BD Scheme adopts φ_C from the downstream cell as the cell interface value. The BD Scheme employs a scheme called Hyper-C.

As shown in Fig. 4(b), when the gas-liquid interface is perpendicular to the cell interface, the volume fraction upstream can be transported downstream with high accuracy. Therefore, the HR Scheme (High Resolution Scheme) employs a high-accuracy upstreaming method called Ultimate QUICKEST.

The normal vector $\mathbf{n}_\varphi$ perpendicular to the gas-liquid interface is calculated from Equation (11). This method is included in the CSF (Continuum Surface Force) method proposed by Brackbill et al. as a method for calculating surface forces as volume forces[11]. However, as discussed later, accurately determining the normal vector of the gas-liquid interface from the volume fraction also presents challenges.

$$\mathbf{n}_\varphi = \frac{\nabla\varphi}{|\nabla\varphi|} \tag{11}$$

Figure 5 shows the calculation results for a Slotted Circle as an example of volume fraction transport calculation. The Slotted Circle method involves setting the initial volume fraction to a circular disk with a notch, as shown in Fig. 5(a), rotating it once, and evaluating whether its shape is maintained.[12] The computational mesh was divided into 35×35 cells, and the volume fraction transport calculation was performed at a uniform angular velocity. The Courant number Cr was set to 0.1, and the calculation was performed using an explicit method. Figure 5(b) shows the results using the first-order upwind scheme, where significant numerical diffusion caused the gas-liquid interface to blur. Figure 5(c) shows the results using the CICSAM method. Although the volume fraction at the boundary exhibits some seepage, it is confirmed that the Slotted Circle shape is maintained.

Figure 6 shows the calculation results for the Slotted Circle with a Courant number Cr of 0.25. Figure 6(a) shows the results using the CICSAM method with the advection term calculated using an explicit method, yielding unnatural results. Figure 6(b) shows the results using the CICSAM method with the advection term calculated using the Crank-Nicolson method, maintaining the shape of the Slotted Circle. Applying the Crank-Nicolson method confirms that

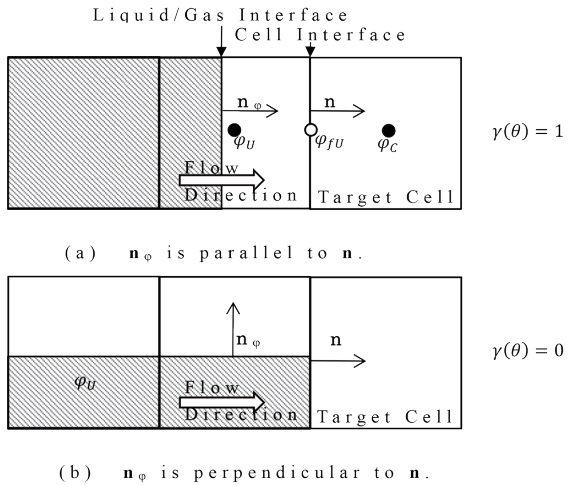

Fig. 4 Schematic diagram of the CICSAM method

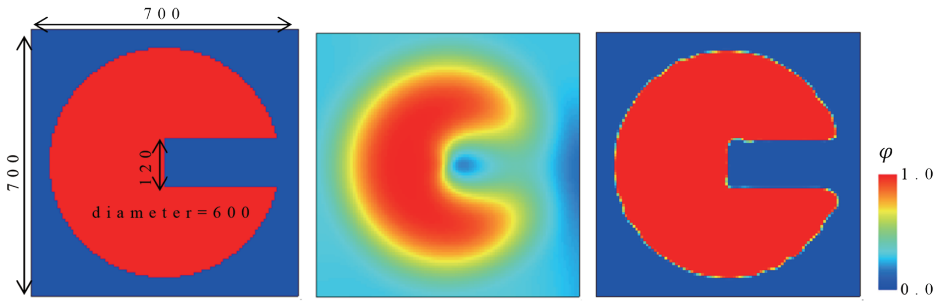

Fig. 5 Calculation results of the slotted circle (Explicit method, Cr=0.1)

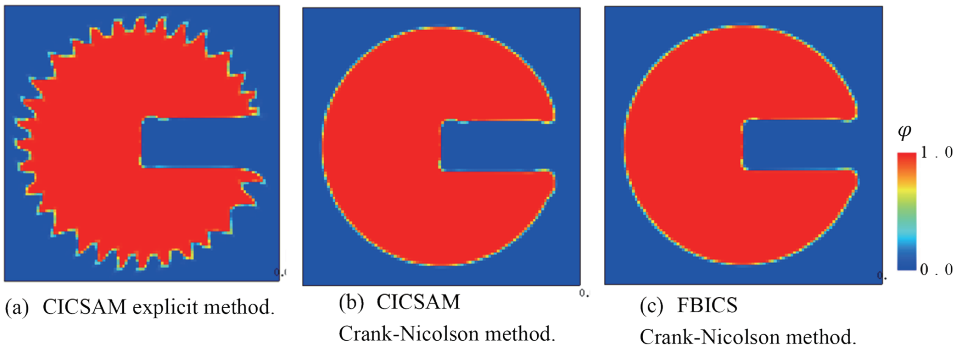

Fig. 6 Calculation results of the slotted circle (Cr=0.25)

reasonable transport calculations of the fluid fraction are possible even at Cr=0.25. Furthermore, Fig. 6(c) shows results calculated using the FBICS method,[13] which is also suitable. While the CIC-SAM method fails to maintain the shape at Cr=0.5 even with the Crank-Nicolson method, the FBICS method successfully preserves the shape at Cr=0.5.

As shown in Fig. 6, transport calculations for the gas-liquid interface using the VOF method appear to be feasible at an acceptable level. However, the fluid fraction in the notched region exhibits seepage, and it is anticipated that the interface will gradually collapse with successive time steps. To address this issue, a process has been proposed to aggregate the dispersed fluid fraction via numerical diffusion. Berberović et al. proposed the third term on the left-hand side of Equation (12) as an interface compression method for transport calculations of the fluid fraction.[14]

$$\frac{\partial \varphi}{\partial t} + \nabla \cdot (\varphi \mathbf{u}) + \nabla \cdot (\varphi (1-\varphi)\, \mathbf{u}_c) = 0 \tag{12}$$

$$\boldsymbol{u}_c = C_\alpha U_f \boldsymbol{n}_f, \quad \boldsymbol{n}_f = \nabla f / |\nabla f| \tag{13}$$

where C_α is a constant.

Takatani proposed the inverse diffusion model in Equation (14) as transport in the opposite direction to conventional diffusion.[15]

$$\frac{\partial \varphi}{\partial t} + \nabla \cdot (\varphi \mathbf{u}) + \nabla \cdot (D_r \nabla \varphi) = 0 \tag{14}$$

$$D_r = C\varphi(1-\varphi)\, C_r (1-C_r), \quad C_r = U_f \Delta t / d \tag{15}$$

Here, C is a constant, and d is the distance between the centers of the symmetric cell and the adjacent cell. Both Berberović et al.'s model and Takatani's model involve transport from cells with low volume fraction to cells with high volume fraction, with the transport amount decreasing as the volume fraction approaches 0 or 1. Takatani's model also accounts for the fact that numerical diffusion is zero when the Courant number is 0 or 1.

2.3 Calculation method for interfacial tension

The force acting at the interface between the gas phase and the liquid phase is called surface tension. At other interfaces, such as liquid/solid, it may be referred to as interfacial tension. This paper describes the gas-liquid interface, but the calculation method is not limited to this, so it is denoted as interfacial tension. Interfacial tension acts with a magnitude equal to the product of the interfacial tension coefficient σ and the curvature k. In the finite volume method, calculations are performed on cells divided into infinitesimal volumes, necessitating the conversion of interfacial tension into a volume force. The CSF method proposed by Brackbill[11] is an excellent technique widely used in many models. For an ideal interface, assuming the interface position is $\boldsymbol{x}_0$, the interfacial tension at position $\boldsymbol{x}$ is expressed using a delta function as shown in Equation (16).

$$F_S = \sigma k \delta (\boldsymbol{x} - \boldsymbol{x}_0) \tag{16}$$

Figure 7(a) shows the distribution of fluid fraction at an ideal interface. Due to numerical diffusion in numerical analysis, the interface cannot be maintained as shown in Fig. 7(a). Instead, the fluid fraction exhibits a gradient distribution over a width Δx, as shown in Fig. 7(b). The CSF method applies the interfacial tension within this gradient range as shown in Equation (17).

$$\mathbf{F}_S = \sigma k \nabla \varphi \tag{17}$$

This method converts interfacial tension into a volume force, enabling its calculation using the finite volume method. Naturally, smaller Δx values allow for higher precision in calculating interfacial tension, and when $\Delta x = 0$, the result matches Equation (16).

Calculating interfacial tension requires curvature k. Curvature is calculated as the divergence of the unit normal vector $\mathbf{n}_S$ in the interfacial direction, using Equation (18).[16]

$$k = \nabla \cdot \boldsymbol{n}_S = \nabla \cdot \frac{\nabla \varphi}{|\nabla \varphi|} = \frac{\varphi_x^2(\varphi_{yy}+\varphi_{zz}) + \varphi_y^2(\nabla_{xx}+\varphi_{zz}) + \varphi_z^2(\varphi_{xx}+\varphi_{yy}) - 2(\varphi_x\varphi_y\varphi_{xy} + \varphi_y\varphi_z\varphi_{yz} + \varphi_z\varphi_x\varphi_{zx})}{(\varphi_x^2+\varphi_y^2+\varphi_z^2)^{\frac{3}{2}}} \tag{18}$$

where $\varphi_{x_i} = \frac{\partial \varphi}{\partial x_i}$ and $\varphi_{ij} = \frac{\partial}{\partial x_j}\frac{\partial \varphi}{\partial x_i}$.

However, it has been reported that the curvature calculated from the volume fraction lacks sufficient accuracy for calculating interfacial tension, and a calculation method using a Level Set function is more suitable.[17] The free surface calculation method combining the VOF method and the Level Set function is called the CLSVOF (Coupled Level Set and Volume Of Fluid) method. The Level Set function ψ (hereafter referred to as the distance function) represents the distance from the interface and satisfies Equation (19).

$$|\nabla \psi| = 1 \tag{19}$$

While tracking the interface is possible by calculating the transport of this distance function using Equation (20), numerical diffusion causes it to no longer satisfy Equation (19), which defines the properties of the distance function.

$$\frac{\partial \psi}{\partial t} + \mathbf{u} \cdot \nabla \psi = 0 \tag{20}$$

To solve this problem, it is necessary to reinitialize the distance function using Equation (21).[18]

$$\frac{\partial \psi}{\partial \tau} + \mathbf{w} \cdot \nabla \psi = S(\psi), \quad \mathbf{w} = S(\psi)\frac{\nabla \psi}{|\nabla \psi|}, \quad S(\psi) = \frac{\psi}{\sqrt{\psi^2 + \delta_c}} \tag{21}$$

Here, τ is the pseudo-time, and δ_C is the grid width. Re-initializing the distance function is sufficient for a few cells near the interface, and specifically, performing about 15 calculations is adequate.[19] The curvature is calculated by substituting the liquid fraction in Equation (18) with the distance function.

Furthermore, the distance function is also used in combination with the Heaviside function to calculate the density and viscosity in cells where gas and liquid phases coexist. In this calculation, this effect was small, so density and viscosity were simply calculated from

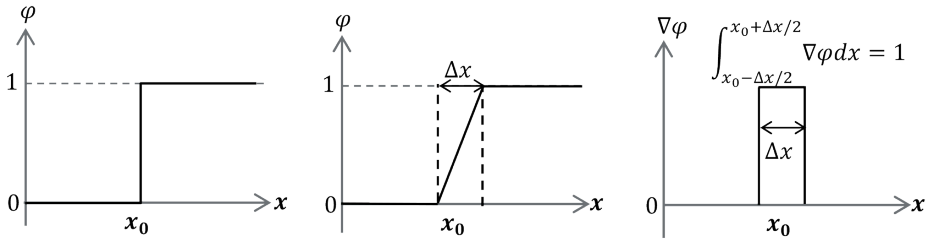

(a) Ideal interface shape (b) Finite volume method (b) Finite volume method

Fig. 7 Distribution of VOF around the interface between the gas and liquid phase

the volume fraction. The Heaviside function is employed in cells where gas and liquid phases coexist to enhance the influence of the denser liquid phase. Applying this concept to interfacial tension calculation yields the density-scaled CSF model, considered essential for milk crown calculations. The interfacial tension in the density-scaled CSF model is given by Equation (22).[19)]

$$\mathbf{F}_S = \frac{\rho}{\frac{1}{2}(\rho_g+\rho_l)}\sigma k\delta_\alpha(\psi)\frac{\nabla\psi}{|\nabla\psi|} \tag{22}$$

Here, ρ_g is the density of the gas phase, and ρ_l is the density of the liquid phase. δ_α is the smoothed delta function, expressed as in Equation (23).

$$\delta_\alpha(\psi) = \begin{cases} \frac{1}{2\alpha}[1+cos(\frac{\pi\psi}{\alpha})] & if\ |\psi|<\alpha \\ 0 & else \end{cases} \tag{23}$$

α is the interfacial evaluation distance, which was set to the grid width.

To aid in understanding the calculation method, **Fig. 8** shows an example of interfacial tension calculation. Figure 8 presents the results of calculating the interfacial tension occurring on a 3 mm radius bubble in a two-dimensional, weightless aquatic environment. Figure 8(a) shows the distribution of the fluid fraction, and Fig. 8(b) shows the distribution of the distance function. The distance function performs reinitialization calculations using the position where the fluid fraction is 0.5 as the interface. Since the distance function is only necessary near the interface, calculations were not performed precisely to the bubble center. The interface calculated from the distance function is shown in the figure. Figure 8(c) shows the curvature calculation result; the curvature of a 3 mm radius bubble is 333, but the distribution is affected by the computational grid. Figure 8(d) shows the final interfacial tension calculated from Equation (22). The direction is not shown but points inward toward the bubble. The density-scaled CSF model confirms that the interfacial tension value on the outer liquid phase side is increased. Applying a large interfacial tension to the low-density gas phase suppresses the generation of unnaturally high flow velocities on the gas phase side.

2.4 Velocity calculation method

The velocity is calculated using Equation (24) after computing the volume fraction transport, employing the density ρ^{n+1} and surface tension $\mathbf{F}_s^{n+1}$ at the next time step. To obtain the velocity $\mathbf{u}^{n+1}$, Equation (25) is used with the predicted value set as $\tilde{\mathbf{u}}$.

$$\frac{\rho^{n+1}\boldsymbol{u}^{n+1}-\rho^n\boldsymbol{u}^n}{\Delta t}+\nabla\cdot(\rho^{n+1}\boldsymbol{u}^n\boldsymbol{u}^n) = -\nabla p^{n+1}+\nabla\cdot(\mu(\nabla\mathbf{u}^n+(\nabla\mathbf{u}^n)^T)+\mathbf{F}_s^{n+1}+\rho^{n+1}\mathbf{g} \tag{24}$$

$$\frac{\rho^{n+1}\tilde{\boldsymbol{u}}-\rho^n\boldsymbol{u}^n}{\Delta t}+\nabla\cdot(\rho^{n+1}\boldsymbol{u}^n\boldsymbol{u}^n) = -\nabla p^n+\nabla\cdot(\mu(\nabla\mathbf{u}^n+(\nabla\mathbf{u}^n)^T)+\mathbf{F}_s^{n+1}+\rho^{n+1}\mathbf{g} \tag{25}$$

Taking the difference between Equation (24) and Equation (25) yields Equation (26).

$$\frac{\rho^{n+1}(\boldsymbol{u}^{n+1}-\tilde{\boldsymbol{u}})}{\Delta t} = -\nabla\delta p \tag{26}$$

Here, δp is the pressure change relative to the previous time step, as shown in Equation (27).

$$\delta p = p^{n+1}-p^n \tag{27}$$

Dividing both sides of Equation (26) by density and then taking the divergence yields Equation (28).

$$\nabla\cdot\boldsymbol{u}^{n+1}-\nabla\cdot\tilde{\boldsymbol{u}} = -\Delta t\nabla\cdot(\frac{1}{\rho^{n+1}}\nabla\delta p) \tag{28}$$

The velocity at the next time satisfies the conservation condition in Equation (4), so $\nabla\cdot\boldsymbol{u}^{n+1}=0$, and Equation (28) becomes Equation (29).

$$\Delta t\nabla\cdot(\frac{1}{\rho^{n+1}}\nabla\delta p) = \nabla\cdot\tilde{\boldsymbol{u}} \tag{29}$$

By calculating Equation (29), the pressure change can be determined, and the velocity at the next time step can be obtained from

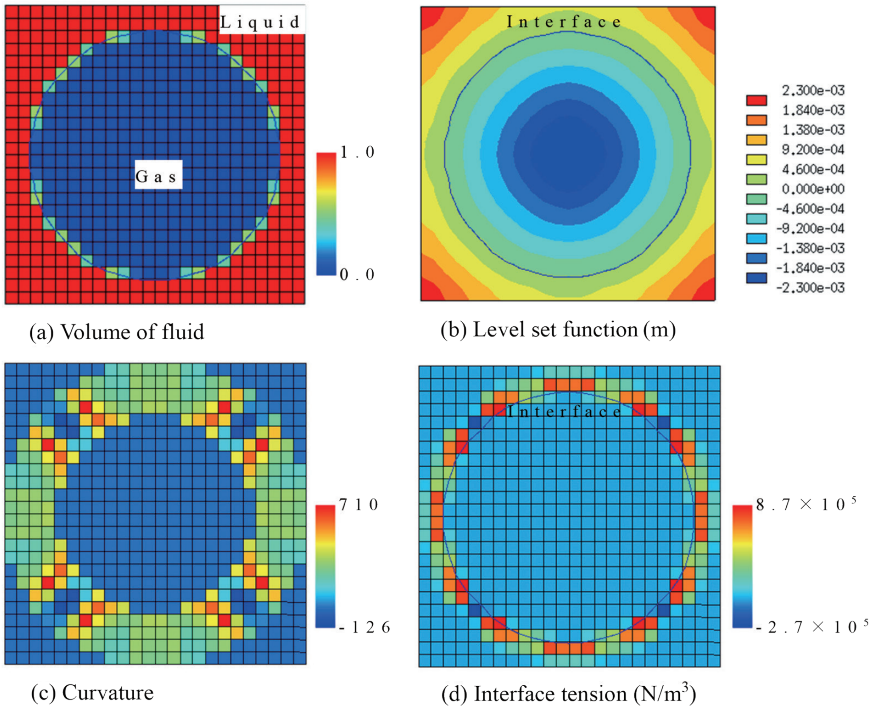

(a) Volume of fluid (b) Level set function (m)

(c) Curvature (d) Interface tension (N/m^3)

Fig. 8 Example of calculation results for interface tension

Equation (26).

Furthermore, to improve the calculation accuracy of the convection term, the Adams-Bashforth scheme[20] is applied as shown in Equation (30). For upstream smoothing of the flow velocity, the quadratic upstream interpolation for convective kinetics (QUICK),[21] which is a second-order accurate scheme, is applied.

$$\nabla\cdot(\rho^{n+1}\boldsymbol{u}^n\boldsymbol{u}^n)=\frac{3}{2}\nabla\cdot(\rho^{n+1}\boldsymbol{u}^n\boldsymbol{u}^n)-\frac{1}{2}\nabla\cdot(\rho^{n}\boldsymbol{u}^{n-1}\boldsymbol{u}^{n-1}) \qquad (30)$$

3. Numerical Analysis Results

The numerical analysis code was developed in C language using a finite volume method for fluid analysis, and parallel computation was performed using Open MPI[22].

Results were compared with those obtained from photographing milk crowns using commercially available milk. A single drop of milk was dropped from a height of 55 cm using a hollow pipette onto a 1 mm thick liquid film of milk poured into a petri dish. This was captured using a high-speed camera operating at 1 000 frames per second.

Numerical analysis employed a computational mesh of 600×600×300 (108 million cells) by dividing a 30×30×15 mm domain into 50 μm intervals. The interfacial tension of milk was set to 5×10^{-2} N/m, the viscosity coefficient to 1.7×10^{-3} Pa·s, and the density to 1 100 kg/m^3. Based on preliminary calculations, Takatani's model was used for the reverse diffusion calculation with a coefficient of 0.0001. From high-speed camera recordings, the diameter of the falling droplet was estimated at 3.6 mm and the droplet velocity at impact at 3.2 m/s; calculations were performed under these conditions. Without considering air resistance, the falling velocity from a height of 55 cm would be 3.28 m/s, which is considered reasonable. However, considering image blur, the falling velocity is estimated to be between 2.9 and 3.2 m/s. Furthermore, although a volume sufficient to form a 1 mm thick liquid film was injected into the petri dish, the film at the impact location was likely thinner than 1 mm due to surface tension.

Figure 9 compares the photographic results of the milk crown with the calculated results. The calculated results display isosurfaces for a volume fraction of 0.5 in three dimensions. To examine the effect of liquid film thickness t, calculations were performed for four levels: 3.0, 1.5, 0.8, and 0.6 mm. Case 4 aimed to approximate the photographic results by setting the falling velocity to v=2.9 m/s.

Figure 9 compares experimental and computational results at 5 ms and 10 ms after the liquid droplet impacts the film, with impact occurring at 0 ms. The experiment used 17 arms, matching the 15 to 17 arms in the numerical analysis. When the liquid film is thick, the cylindrical section exhibits a flared shape. Since the experimental results show the cylindrical section is nearly perpendicular to the liquid surface, the shape in Case 4 (0.6 mm film thickness) is closer

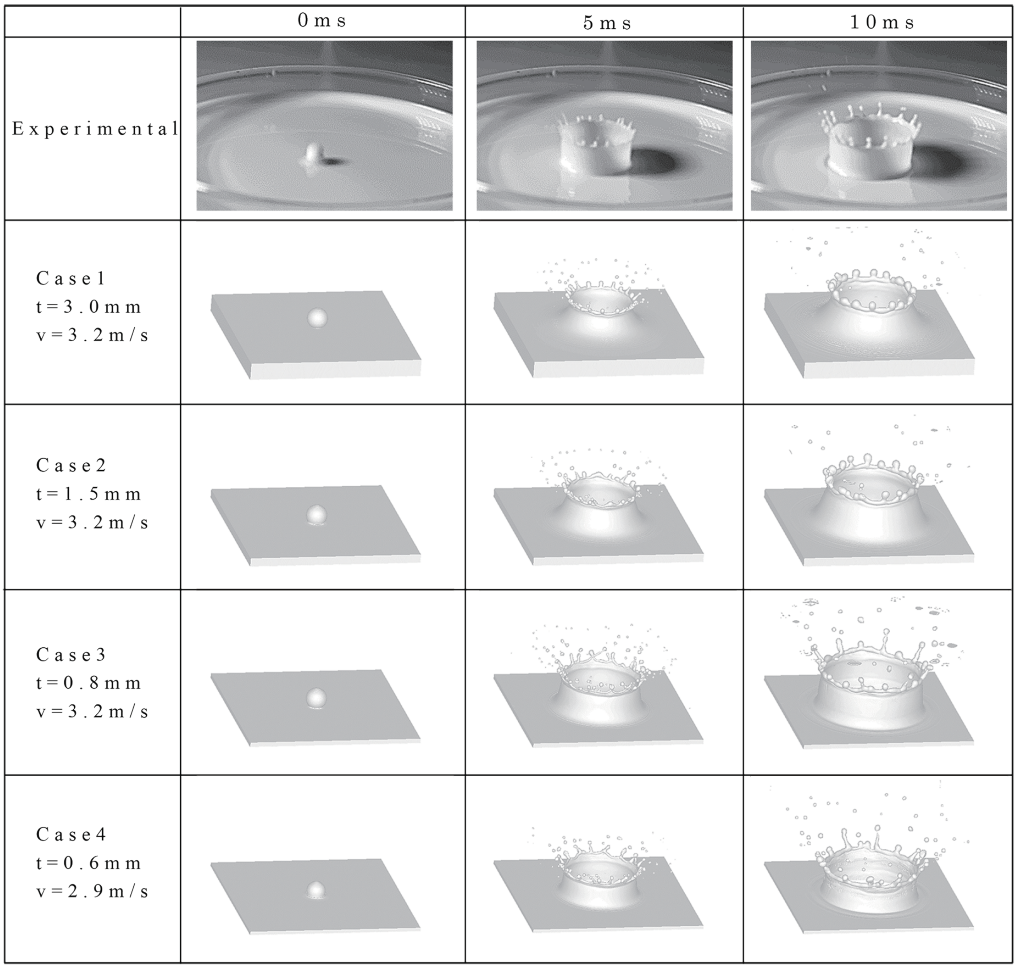

Fig. 9 Comparison of the experimental results and numerical results

to the experimental results. However, while the experimental milk crown shows the cylindrical section growing taller between 5 ms and 10 ms, the cylindrical height in Case 4 does not increase. Both the experimental results and Case 3 show the cylindrical section increasing in height between 5 ms and 10 ms, confirming that collision velocity significantly affects the cylinder height. While Case 3 in this calculation yielded results closest to the experiment, conditions intermediate between Case 3 and Case 4 are thought to better match the experimental results. Thus, although this comparison lacks quantitative precision, it confirms that actual milk crowns can be reproduced through numerical analysis.

Figure 10 shows the results of calculations performed under the experimental conditions of Terzis et al.[4] for a urea aqueous solution. The droplet diameter is 2.1 mm, the falling velocity is 4.26 m/s, the interfacial tension is 7.28×10^{-2} N/m, the viscosity coefficient is 1.37×10^{-3} Pa·s, the liquid film thickness is 0.252 mm, the density is 1 083 kg/m^3, and the We number is 560. The computational domain was 15 mm × 15 mm × 5.0 mm, with a grid spacing of 37.5 μm, and

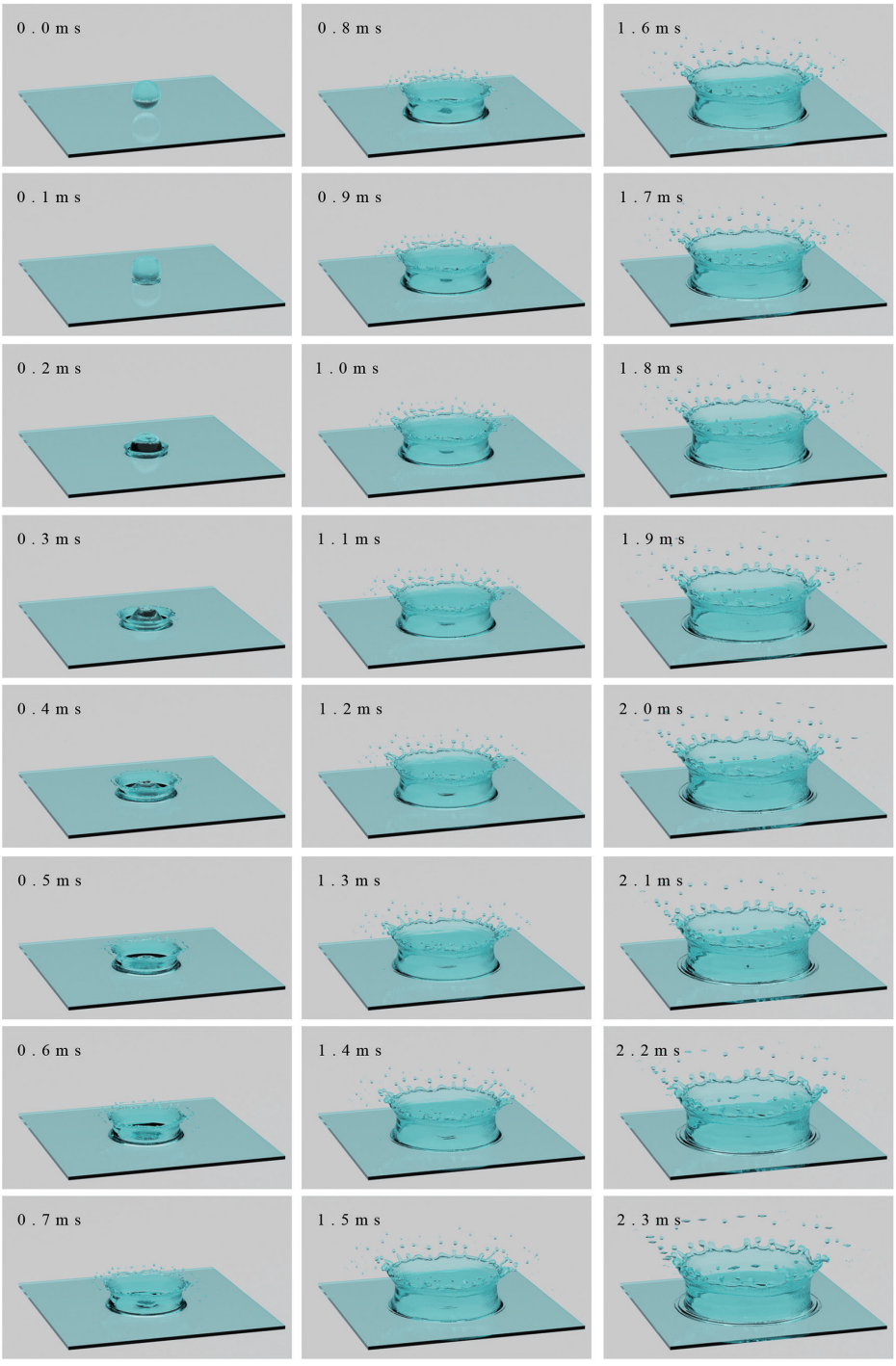

Fig. 10 Calculation results of milk crown for the urea-water solution

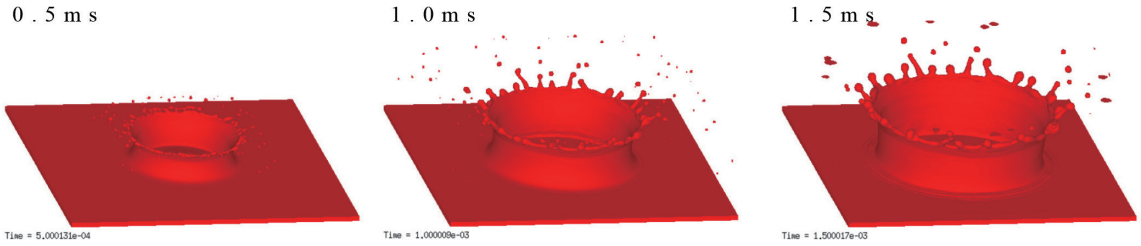

Fig. 11 Calculation results of milk crown for molten steel

approximately 20 million mesh calculations were performed.

Figure 10 shows that for approximately 0.5 ms after the droplet impacts the liquid film, the cylindrical liquid film bulges, generating minute droplets. Subsequently, by approximately 1 ms, the thickness of the upper end of the cylinder increases, and the protrusion grows to form an arm. Around 1.5 ms, a spherical droplet separates from the tip of the protrusion, forming a milk crown. At 2.3 ms, the droplet reaches the upper edge of the computational domain.

The number of arms confirmed from the calculation results is 25, matching the 26 arms reported in Terzis et al.'s[4] experimental results. The shape of the milk crown closely matched the photographs reported by Terzis.

Figure 11 shows the results calculated with the droplet properties set to molten steel and the same We number as the urea solution in Fig. 10. The droplet and liquid film properties were set to the same values. The density of molten steel was set to 7000 kg/m^3, the interfacial tension to 1.0 N/m, and the falling velocity to 6.18 m/s to achieve the same We number of 560.

Figure 11 confirms that, for the same We number, the crown shape closely resembles that of the urea solution. However, due to the higher impact velocity and greater density, the velocity of the minute spray droplets was faster than that observed in the urea solution. Molten steel splatter is often evaluated using water models and categorized by We number. In this case, while the concave and convex shapes are considered similar, the differing distances of the droplets are a concern.

4. Summary

We attempted to reproduce the natural phenomenon known as the milk crown through numerical analysis. Reproducing this phenomenon, occurring over just a few square centimeters for a few milliseconds, required numerous techniques and substantial computational resources. The insights gained will be incorporated into future analyses of multiphase flow processes. Numerical analysis of large-scale processes in the iron and steel industry cannot realistically perform calculations as intricate as those for the milk crown. Therefore, it is necessary to extract key phenomena, model them, and obtain solutions within a practical computational time. Identifying these key phenomena is considered the essence of numerical analysis, as it enables an understanding of the process's fundamental nature.

References

1) Worthington, A.M.: A Study of Splashes. Longmans Green and Company, London, 1908
2) https://mitmuseum.mit.edu/collections/object/HEE-NC-57001
3) Deegan, R.D., Brunet, P., Eggers, J.: Complexities of splashing. Nonlinearity. 21 (1), C1 (2008)
4) Terzis, A., Kirsch, M., Vaikuntanathan, V., Geppert, A., Lamanna, G., Weigand, B.: Experimental Thermal and Fluid Science. 102, 152 (2019)
5) Yokoyama, M., Murotani, K., Yagawa, G.: Computational Particle Mechanics. 6, 249 (2019)
6) Inamuro, T., Yoshino, M., Suzuki, K.: Introduction to Lattice Boltzmann Methods. Maruzen Publishing, Tokyo, 2020
7) Hirt, C.W., Nichols, B.D.: Journal of Computational Physics. 39, 201 (1981)
8) Sethian, J.A.: Level Set Method and Fast Marching Methods. 2nd ed. Cambridge University Press, Cambridge, 1999
9) Osher, S., Fedkiw, R.: Level Set Methods and Dynamic Implicit Surface. Springer-Verlag, New York, 2003
10) Ubbink, O., Issa, R.: J. Comput. Phys. 100, 25 (1992)
11) Brackbill, J.U., Kothe, D.B., Zemach, C.: J. Comput. Phys. 100, 335 (1992)
12) Heyns, J.A., Malan, A.G., Harms, T.M., Oxtoby, F.: Int. J. Numer. Meth. Fluid. (2012), DOI:10.1002/fld.3694
13) Tsui, Y.Y., Lin, S.W., Cheng, T.T., Wu, T.C.: Int. J. Heat and Mass Transfer. 52, 5547 (2009)
14) Berberović, E., van Hinsbergs, N.P., Jakirlić, S., Roisman, I.V., Tropea, C.: The American Physical Society. 79, 036306 (2009)
15) Takatani, K.: ISIJ Int. 47, 545 (2007)
16) Croce, R.: Ein paralleler, dreidimensionaler Navier-Stokes-Löser für inkompressible Zweiphasenströmugen mit Oberächenspannung, Hindernissen und dynamischen Kontaktflächen. Diplomarbeit, Rheinischen Friedrich-Wilhelms-Universität Bonn, (2002)
17) Tomiyama, A., Sakoda, K., Hayashi, K., Sou, A., Shimada, N., Hosokawa, S.: Modeling Hybrid Simulation of Bubbly Flow. Japan-US Seminar on Two-Phase Dynamics, December 6-11, 2004, Nagahama, Japan
18) Sussman, M., Smereka, P., Osher, S.: J. Comput. Phys. 146, 114 (1994)
19) Yokoi, K.: J. Comput. Phys. 232, 252 (2013)
20) Kobayashi, T. (ed.): Handbook of Computational Fluid Dynamics. Tokyo, Maruzen, 2003, p.35
21) Leonard, A.: Adv. Geophys. 18A, 237 (1974)
22) https://www.open-mpi.org/

Nobuhiro OKADA
Ph.D., General Manager, Head of Dept.
Mathematical Science & Technology Research Lab.
Advanced Technology Research Laboratories
20-1 Shintomi, Futtsu City, Chiba Pref. 293-8511

Kouji TAKATANI
Ph.D., Former Advisor